ChemSusChem

Research Article
doi.org/10.1002/cssc.202500999

Chemistry Europe
European Chemical Societies Publishing

www.chemsuschem.org

VIP *Very Important Paper*

Ca^{2+}-Driven Enhancement of Anodic Performance and Sulfur Utilization for Magnesium–Sulfur Batteries

Reona Iimura,* Sibylle Riedel, Hiroaki Kobayashi,* Masaki Matsui, Itaru Honma, Maximilian Fichtner, and Zhirong Zhao-Karger*

Magnesium–sulfur (Mg–S) batteries are emerging as promising energy storage systems due to their cost-effectiveness, safety, and high theoretical volumetric energy density. However, their practical implementation is hindered by sluggish sulfur redox kinetics with Mg^{2+} and severe polysulfide shuttling. Here, a double-divalent Mg–Ca hybrid electrolyte is introduced, where a small amount of Ca^{2+} additive significantly enhances sulfur redox kinetics, leading to higher sulfur utilization. Notably, Ca^{2+} primarily facilitates the solid-to-solid conversion of disulfide to sulfide. In addition to the cathode reaction, the Mg–Ca hybrid electrolyte also contributes to the anode reaction; it enables smoother Mg plating and reduces overpotential with the long cycle (>1000 cycles). For mitigating the polysulfide shuttling, the glass fiber separator with ultrasmall α-MnO_2 nanoparticles is modified to adsorb polysulfide. This synergistic strategy of electrolyte and separator engineering enables the Mg–S battery to achieve an initial capacity exceeding 1000 mAh g^{-1} and extended cycling stability. These findings highlight the potential of Mg–Ca hybrid electrolytes and nanosized α-MnO_2-modified separators in the development of high-performance Mg–S batteries.

1. Introduction

To support an increasingly electrified society driven by the widespread adoption of electric vehicles and smart grids, it is crucial to explore complementary options to conventional lithium-ion batteries (LIBs).[1] Moreover, the development of energy storage systems utilizing cost-effective and sustainable materials is essential to address challenges arising from current economic and material supply chain uncertainties. In this context, rechargeable magnesium batteries (RMBs) have emerged as a promising solution for sustainable energy storage, offering several advantages, including cost-effectiveness, improved safety, and high volumetric energy density.[2–4] When paired with a sulfur cathode, which possesses a high theoretical capacity (1672 mAh g^{-1}, 3459 mAh L^{-1}), RMBs have the potential to deliver high-energy-density storages (up to 3250 Wh L^{-1}).[5,6]

A significant challenge in magnesium–sulfur (Mg–S) batteries is the sluggish sulfur conversion reaction kinetics with Mg^{2+}.[7] This is primarily due to sulfur's extremely low electrical conductivity (5×10^{-30} S m^{-1})[8] and the high charge density of Mg^{2+} (120 C mm^{-3}, compared to 52 C mm^{-3} for Li^+).[9] These unfavorable kinetics lead to low sulfur utilization and substantial voltage hysteresis.[10,11] To address the issue of low conductivity, many researchers have focused on enhancing charge transfer within the sulfur cathode by incorporating a high proportion of conductive carbon into the sulfur matrix[12–15] or utilizing activated carbon cloth as a current collector.[16,17] These approaches significantly improve charge transfer to sulfur, facilitate efficient redox reactions with Mg, and achieve superior sulfur-based capacity. However, the use of large amounts of conductive carbon reduces energy density, making these strategies unsuitable for practical Mg–S battery systems.[18]

To improve the intrinsic reaction kinetics of sulfur, our group recently developed a solid-solution cathode $S_{1-x}Se_x$ with enhanced electrical conductivity achieved through selenium incorporation.[19] This advancement leads to higher sulfur utilization and reduced voltage hysteresis. While the initial voltage curve closely aligns with theoretical predictions, the subsequent capacity declines rapidly due to the dissolution of polyselenides and polysulfides, resulting in insufficient electrical conductivity of sulfur.

To further improve the reaction kinetics of the sulfur cathodes, electrolyte regulation approaches have proven effective. Some studies have incorporated Li salts into Mg electrolytes, leveraging the monovalent cations to facilitate sulfur redox reactions.[20,21] In particular, an electrolyte consisting of 0.1 M Mg-HMDS + 1.0 M

R. Iimura, I. Honma
Institute of Multidisciplinary Research for Advanced Materials
Tohoku University
Sendai 980-8577, Japan
E-mail: reona.iimura.r5@dc.tohoku.ac.jp

R. Iimura, S. Riedel, M. Fichtner, Z. Zhao-Karger
Helmholtz Institute Ulm (HIU)
89081 Ulm, Germany
E-mail: zhirong.zhao-karger@kit.edu

R. Iimura, M. Fichtner, Z. Zhao-Karger
Institute of Nanotechnology (INT)
Karlsruhe Institute of Technology (KIT)
76344 Karlsruhe, Germany

R. Iimura, H. Kobayashi, M. Matsui
Department of Chemistry, Faculty of Science
Hokkaido University
Sapporo 060-0810, Japan
E-mail: h.kobayashi@sci.hokudai.ac.jp

Supporting information for this article is available on the WWW under https://doi.org/10.1002/cssc.202500999

LiTFSI/G4 (HMDS: hexamethyldisilazide, TFSI: trifluoromethanesulfonimide, G4: tetraethylene glycol dimethyl ether) has demonstrated reversible sulfur redox with a capacity of up to 1000 mAh g^{-1}, attributed to the assisting effect of Li^+.[22] However, from a thermodynamic perspective, equilibrium voltage for E_{MgS} for the reaction $S + Mg \rightarrow MgS$ is calculated to be 1.77 V, which is higher than E_{MLS} of 1.62 V based on the Li^+-driven reaction $S + Mg + 2Li^+ \rightarrow Li_2S + Mg^{2+}$ as previously reported.[21] This suggests that although Li^+ ions promote the reversibility of sulfur redox reactions in Mg–Li hybrid systems, the reaction is thermodynamically less favorable—requiring a relatively high concentration of Li^+ to proceed effectively. Furthermore, relying on monovalent cations to assist sulfur redox can lead to significant sulfur volume expansion (e.g., Li_2S: 80%, Na_2S: 170%), which undermines the practicality of this approach for sustainable cell designs.[6]

Other studies have focused on separator modifications to prevent polysulfide migration to the anode to improve cycling stability. Examples include Mo_6S_8-modified separators,[23] decavanadate-based polyoxometalate (POM) clusters/carbon composite modification,[24] and carbon nanofiber (CNF) coating modification.[25] These modifications have demonstrated a certain degree of effectiveness in extending cycle life. However, such approaches require a substantial amount of modification materials, which increases the overall battery weight, potentially limiting their practicality.

In this study, we explored the addition of Ca salts to Mg electrolytes as a strategy to enhance sulfur redox kinetics and a separator modification with single-nanosized α-MnO_2 for prolonging cycle life. In the former part, Ca^{2+}, a divalent ion with almost the same charge density as Li^+, is expected to facilitate sulfur redox reactions even in smaller quantities compared to Daniel-type Mg–Li dual-cation battery systems. Indeed, thermodynamic calculations (see Supporting Information) indicate a higher equilibrium voltage E_{MCS} of 1.92 V for the reaction $S + Mg + Ca^{2+} \rightarrow CaS + Mg^{2+}$, where Ca^{2+} exclusively drives the sulfur conversion. This suggests that the Mg–Ca hybrid electrolyte system can promote sulfur redox thermodynamically with only small amounts of additive cations. As an electrolyte additive, we introduced $Ca[B(hfip)_4]_2$ (hfip: hexafluoroisopropyl) into the $Mg[B(hfip)_4]_2$/DME (DME: dimethoxyethane) electrolyte system. The $[B(hfip)_4]^-$-based electrolyte is well known for its high metal stripping-plating efficiency and wide electrochemical stability window for both Mg and Ca battery applications.[16,26] Since no previous studies have reported double-divalent hybrid electrolyte systems, we firstly investigated the impact of the Mg–Ca hybrid electrolyte on the Mg anode. Our findings revealed that the Ca salt additive enables prolonged cycling with reduced overpotential and promotes uniform and smooth Mg plating at stripped sites. On the sulfur cathode side, the discharge capacity and sulfur reaction kinetics were significantly improved, with new voltage plateaus attributed to the conversion of polysulfide and sulfides due to the Ca^{2+} supporting effect. In the latter part, we implemented a separator modification with single-nanosized α-MnO_2, inspired by the high polysulfide adsorption of α-MnO_2 in Li–S batteries.[27,28] Recently, we have reported the single-nanoparticulated α-MnO_2 with a high specific surface area, which can adsorb more polysulfides than conventional α-MnO_2.[29] In this study, we directly incorporated it into a glass fiber separator (GF/C) using a wet-process, without any binders. This modified separator is expected to effectively suppress polysulfide migration to the anode by utilizing the large active surface area of α-MnO_2, while simultaneously reducing the required amount of polysulfide absorbent, enabling long-term cycling with high sulfur utilization when used in conjunction with the Mg–Ca hybrid electrolyte.

2. Results and Discussions

2.1. Smooth Mg Plating with $Mg[B(hfip)_4]_2$ Electrolyte Containing $Ca[B(hfip)_4]_2$ Additive

To evaluate the compatibility of the Mg anode with the Mg–Ca hybrid electrolyte, as well as its polarization behavior and long-term stability at typical cathode operating current densities, galvanostatic cycling tests were conducted using an Mg||Mg symmetric cell. As shown in the inset of **Figure 1**a, $Mg[B(hfip)_4]_2$/DME-based electrolytes exhibited high initial polarization. With a higher concentration (Mg:Ca = 2:1) of $Ca[B(hfip)_4]_2$, a even larger polarization was observe. This high initial polarization is primarily attributed to an adsorption layer formation by electrochemically inactive species on the Mg anode surface, as reported in previous studies.[30,31] Additionally, solvated $[Ca(DME)_4]^{2+}$ may hinder Mg stripping and plating, leading to polarization increase. Furthermore, potentiostatic electrochemical impedance spectroscopy (EIS) measurements (Figure S1, Supporting Information) revealed that the 0.3 M $Mg[B(hfip)_4]_2$ + 0.15 M $Ca[B(hfip)_4]_2$/DME electrolyte exhibited 1.25 times higher charge transfer resistance at open-circuit voltage (OCV) compared to the pure Mg electrolyte, which likely contributes to the high initial polarization observed during galvanostatic cycling.

During the initial few cycles, a relatively large polarization of approximately ±0.3 V was observed for Mg plating and stripping. On the other hand, the polarization gradually decreased with continued cycling and stabilized in the range of ±0.1 V to ±0.12 V. Notably, 0.3 M $Mg[B(hfip)_4]_2$ + 0.05 M $Ca[B(hfip)_4]_2$/DME electrolyte took a shorter stabilization time (from 20 to 8 cycles for ±0.1 V stabilization) and lower Mg stripping/plating polarization over 1000 cycles; this behavior became more pronounced at higher $Ca[B(hfip)_4]_2$ concentrations, indicating that the activation of the Mg/electrolyte interface is quicker than pure Mg electrolyte, forming a suitable interface for Mg stripping/plating. Furthermore, $Ca[B(hfip)_4]_2$ additive is also effective for high-rate Mg striping/plating, as shown in Figure S2, Supporting Information. At all current densities, Mg–Ca hybrid electrolyte exhibited smaller polarization.

Cyclic voltammetry (CV) studies of the Mg–Ca hybrid electrolytes were conducted using two-electrode cells with stainless steel (SS) as the working electrode, and the CV curves are presented in Figure 1b,c, and S3a. At the first cycle, cathodic and anodic currents are suppressed by Ca^{2+} concentration, suggesting that Ca^{2+} hinders electrochemical reactions not only on the Mg surface but also on the SS surface. After several cycles, cathodic and anodic peak currents reached nearly 40 mA cm^{-2} with the Mg–Ca hybrid electrolytes, ≈1.5 times higher than the pure Mg electrolyte. The coulombic efficiency using an Mg||Cu asymmetric cell was

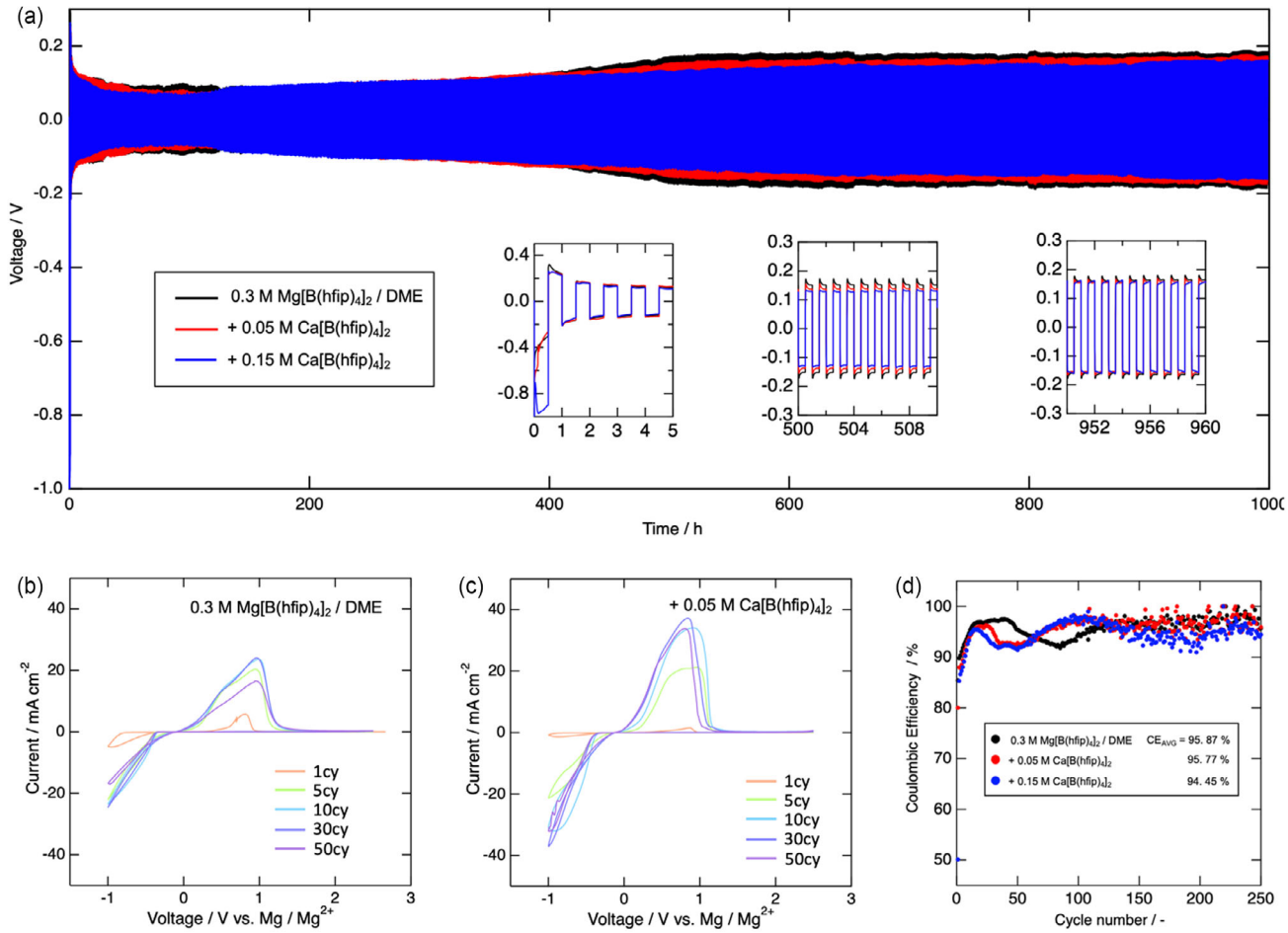

Figure 1. a) The polarization properties of Mg||Mg cells at 0.1 mA cm^{-2} and 0.05 mAh cm^{-2}. Inset: enlarged profiles at different time scale. CVs for Mg plating and stripping in Mg||SS cell at 25 mV s^{-1} with b) 0.3 M $Mg[B(hfip)_4]_2$/DME, c) 0.3 M $Mg[B(hfip)_4]_2$ + 0.05 M $Ca[B(hfip)_4]_2$/DME, and d) Coulombic efficiency from asymmetrical Mg||Cu cell at 0.1 mA cm^{-2} and 0.1 mAh cm^{-2}.

calculated based on charge balance from galvanostatic cycling (Figure 1d). The initial coulombic efficiency was lower at higher Ca^{2+} concentrations but improved with each cycle, eventually stabilizing near 95%, with detailed profiles presented in Figure S4, Supporting Information. Note that the charge balance is also calculated from CV (Figure S3b, Supporting Information), resulting in a similar trend. In particular, the 0.3 M $Mg[B(hfip)_4]_2$ + 0.05 M $Ca[B(hfip)_4]_2$/DME electrolyte demonstrated a high coulombic efficiency comparable to that of the pure Mg electrolyte while exhibiting superior Mg stripping/plating behavior. As shown in Figure S4d, Supporting Information, this hybrid electrolyte displayed a longer Mg re-plating plateau than the pure Mg electrolyte, suggesting a homogeneous reaction with rapid Mg plating kinetics.

To further investigate the influence of $Ca[B(hfip)_4]_2$, the surface morphology of the Mg anode during Mg stripping/plating was examined. **Figure 2**a,e present scanning electron microscopy (SEM) images of the Mg anode in its fully stripped state, using 0.3 M $Mg[B(hfip)_4]_2$/DME electrolyte with and without 0.05 M $Ca[B(hfip)_4]_2$ additive. No noticeable differences were observed between the two conditions, as both exhibited similar Mg-stripped holes. However, significant differences emerged at the half Mg re-plating state. In the pure Mg electrolyte, Mg deposition occurred within the glass fiber separator on the anode side instead of within the stripped holes, as shown in Figure 2b,c. Based on the previous papers,[32–34] this phenomenon is explained as follows: 1) the replated, thin Mg grows three-dimensionally toward the glass fiber separator; 2) these thin, plate-shaped Mg deposits continuously detach from the anode and become trapped within the glass fiber structure.

In contrast, no Mg deposition was observed in the glass fiber separator when 0.05 M $Ca[B(hfip)_4]_2$ was added to the electrolyte (Figure 2g). Instead, plate-shaped Mg was deposited inside the stripped holes (Figure 2f). As shown in Figure S5a, Supporting Information, electrolytes with higher Ca concentrations also promoted the formation of plate-shaped Mg within the stripped holes. Notably, with 0.15 M $Ca[B(hfip)_4]_2$, the replated Mg plates were even thicker. The thickness of deposited Mg plates is ≈400 nm with 0.05 M $Ca[B(hfip)_4]_2$ and 600 nm with 0.15 M $Ca[B(hfip)_4]_2$. These plate-like Mg structures expose a (001) plane, and an increase in thickness suggests a greater presence of (101) and (100) planes. The presence of Ca^{2+} inhibits the nucleation of Mg on the (001) plane; instead, it promotes the growth of the (101) and (100) planes, resulting in thicker Mg deposits. This

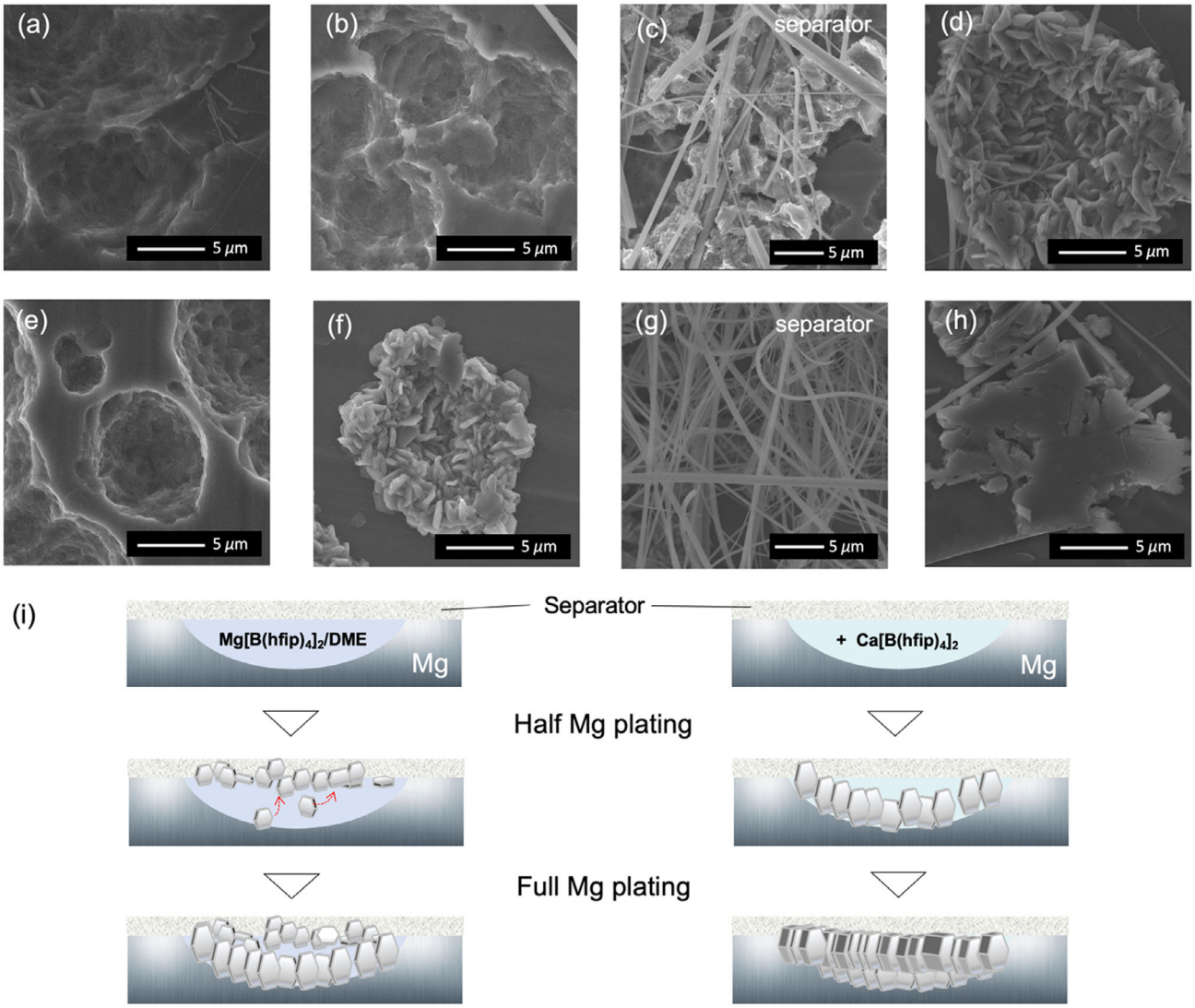

Figure 2. SEM images of a,e) Mg anode at fully Mg-stripped state (0.1 mA cm^{-2}, 0.5 mAh cm^{-2}) b,f) Mg anode at half Mg-plated state (0.1 mA cm^{-2}, 0.25 mAh cm^{-2}), c,d) separator of anode side at half Mg-plated state, and d,h) Mg anode at fully Mg-plated state (0.1 mA cm^{-2}, 0.5 mAh cm^{-2}). Note that (a)–(d) are with 0.3 M $Mg[B(hfip)_4]_2$/DME and (e)–(h) are with 0.3 M $Mg[B(hfip)_4]_2$ + 0.05 M $Ca[B(hfip)_4]_2$/DME. i) Estimated mechanism for Mg plating to stripped sites with or without $Ca[B(hfip)_4]_2$ addition to the electrolyte.

suggests that, under the same current densities, Ca^{2+} additives alter Mg deposition behavior from the thermodynamically stable orientation, the (001) plane, toward kinetically favored orientations, such as the (101) and (100) planes.[35] Since the (101) plane has higher absorption energy,[36] the thicker plate-shaped Mg deposits should adhere to the Mg anode strongly, effectively preventing detachment from the stripped sites and subsequent migration into the separator. This unique plating mechanism can be classified as "cationic shield-mediated electrodeposition," as described in a previous study.[37] In hybrid electrolyte systems, the additive cations tend to physically adsorb onto dendrite tips, forming an electrostatic shield that significantly suppresses dendritic growth. For example, in sodium metal battery systems using a Na–K hybrid electrolyte, Na dendrite growth was effectively mitigated by the electrostatic shielding effect of K^+ ions.[38]

At the fully Mg re-plated state, plate-shaped Mg was observed in the pure Mg electrolyte (Figure 2d); however, its thickness was less than 200 nm, thinner than that using Ca-added electrolyte. In contrast, with the addition of $Ca[B(hfip)_4]_2$, the plated Mg exhibited a flat and smooth morphology, as shown in Figure 2h and S5b, Supporting Information. To further understand the growth mechanism of the flat and smooth Mg, Mg plating onto a Cu substrate was investigated using 0.05 M $Ca[B(hfip)_4]_2$ added electrolyte (Figure S6, Supporting Information). A comparison between the half-plated and fully plated states revealed that the plate-shaped Mg deposits grew among the pre-existing plated Mg, merging and forming a continuous, flat, and smooth Mg layer. A similar Mg plating should occur within the stripped hole on the Mg anode. The observed Mg plating behaviors are summarized in Figure 2i. Note that no Ca has been detected in SEM energy dispersive X-ray spectroscopy (EDX) measurements at the fully Mg re-plated state with 0.15 M $Ca[B(hfip)_4]_2$ additives, as shown in Figure S7, Supporting Information.

2.2. Mg–S Battery Cell Performance with $Ca[B(hfip)_4]_2$ Added Electrolyte

To investigate the effect of the Mg–Ca hybrid electrolyte on a practical sulfur cathode, a sulfur (S), Ketjenblack (KB), and Super P composite (SKB) were prepared via ball milling without any additional heat treatment. Figure S8, Supporting Information, presents X-ray diffraction (XRD) patterns, a SEM image, and EDX maps of the SKB composite. The XRD pattern of the SKB shows no distinct diffraction peaks of sulfur; broad peaks originating from KB were observed. This result is consistent with previous study,[19] indicating that high-energy ball milling produces amorphous or nanosized sulfur. Additionally, SEM imaging and EDX mapping confirmed that the SKB composite consisted of single-micro-sized particles, with sulfur uniformly distributed across KB and Super P.

The galvanostatic discharge/charge profiles of Mg–S cells with pure Mg electrolyte is presented in Figure S9a, Supporting Information. It delivered a first discharge capacity of 491 mAh g^{-1}, a significantly low value compared with the theoretical capacity (1675 mAh g^{-1}). During the initial cycles, the discharge profile exhibited a relatively flat voltage plateau at ≈1.2 V, followed by a second plateau near the cut-off voltage of 0.5 V. According to previous mechanistic analysis using $Mg[B(hfip)_4]_2$ electrolytes,[16] the first plateau corresponds to the redox reaction of sulfur to polysulfides (MgS_x, $x = 2, 4, 6, 8$), while the second plateau is primarily attributed to the conversion of polysulfide to sulfide (MgS). This latter reaction is particularly sluggish due to containing the solid-to-solid (MgS_2–MgS) phase transition.[39] During the charging process, a long and flat voltage plateau was observed at 2.1–2.2 V, indicating the presence of severe polysulfide shuttle behavior.[21] Regarding the 2nd and 3rd cycles, discharge and charge capacity were decreased mainly due to polysulfide dissolution to the electrolyte.

On the other hand, the Mg–S cells with the electrolyte containing additional $Ca[B(hfip)_4]_2$ exhibit a significant discharge capacity enhancement as shown in Figure S9b,c, Supporting Information. The addition of 0.05 M $Ca[B(hfip)_4]_2$ resulted in a first discharge capacity of 775 mAh g^{-1}, while 0.15 M $Ca[B(hfip)_4]_2$ further increased it to 814 mAh g^{-1}. These capacity improvements were primarily attributed to the long voltage plateau around 1.0 V. Previous studies on systems with improved sulfur reaction kinetics, such as $S_{1-x}Se_x$ cathodes,[19] have reported a rise in the second plateau potential. Therefore, the $Ca[B(hfip)_4]_2$ addition facilitates the reaction kinetics in the solid-to-solid phase transition, resulting in the 0.5 V upshift of the second plateau.

As shown in the summarized voltage profiles and *dQ*/*dV* plots in **Figure 3**a and S10, the second plateau potential shifts higher as the concentration of $Ca[B(hfip)_4]_2$ in the electrolyte increases, accompanied by an increase in discharge capacity. On the other hand, the amount of $Ca[B(hfip)_4]_2$ additive does not appear to influence the discharge capacity of the first plateau (around 1.2 V). These results

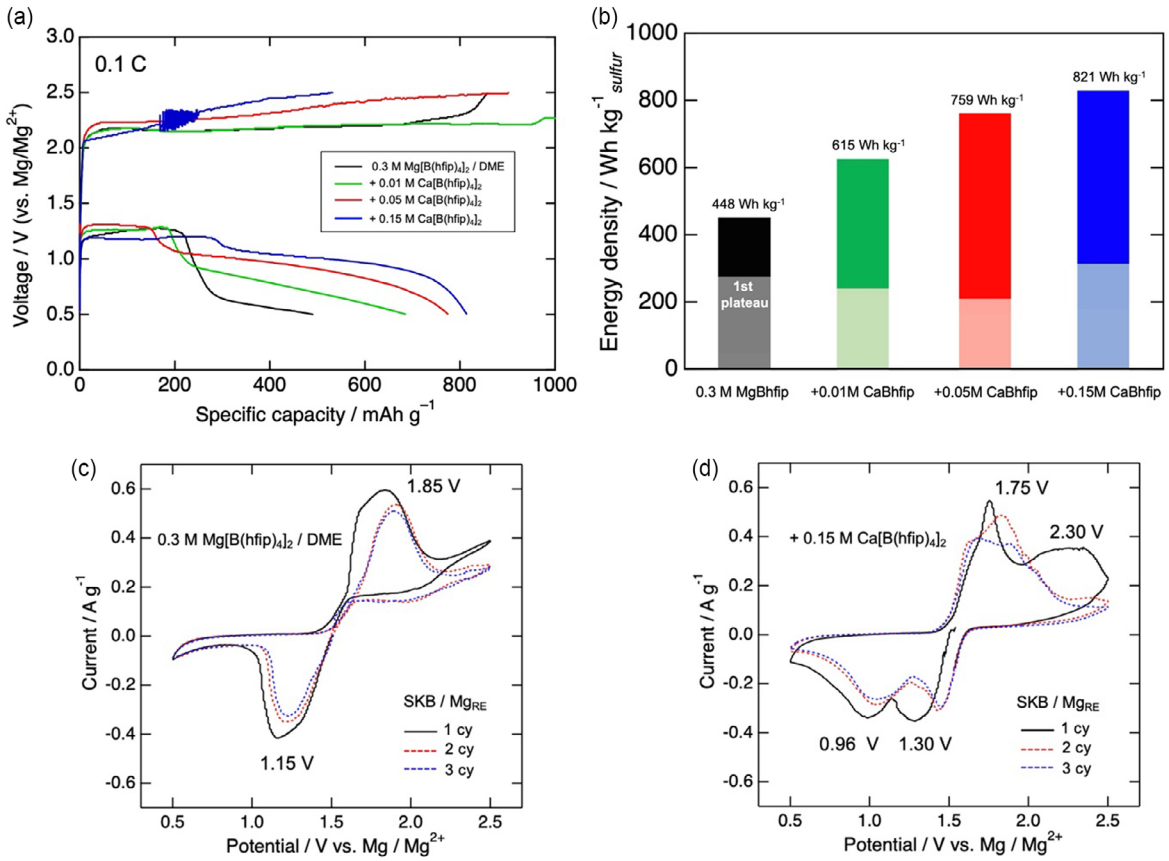

Figure 3. a) 1st voltage profile of Mg–S cells at 0.1 C with different concertation of $Ca[B(hfip)_4]_2$/DME. b) Energy density per unit sulfur mass calculated from 1st discharge profile, CVs of Mg–S cells in a three electrode set up (WE: SKB, CE: Mg and RE: Mg) at 0.1 mV s^{-1} with c) 0.3 M $Mg[B(hfip)_4]_2$/DME and d) 0.3 M $Mg[B(hfip)_4]_2$ + 0.15 M $Ca[B(hfip)_4]_2$/DME.

suggest that $Ca[B(hfip)_4]_2$ primarily facilitates the latter stages of the solid-state sulfur redox reaction, particularly the conversion of disulfide to sulfide. Figure 3b presents the energy density per unit sulfur mass, calculated from the first discharge profile. Due to the upward shift of the second plateau voltage resulting from $Ca[B(hfip)_4]_2$ addition, the energy density was significantly improved. Especially, the addition of 0.15 M $Ca[B(hfip)_4]_2$ enabled an energy density over 1.8 times higher than that achieved with the pure Mg electrolyte.

At the charging process (Figure S9b,c, Supporting Information), no significant improvements in charge behavior were observed, likely due to the high anodic overpotential during the first cycle, as shown in Figure 1a. Furthermore, the addition of 0.15 M $Ca[B(hfip)_4]_2$ introduced undesirable noise around 2.2 V, possibly due to the high resistive layer at the Mg anode, and resulted in incomplete charging relative to the observed discharge capacity. Additionally, the effect of $Ca[B(hfip)_4]_2$ persisted in the second, third, and subsequent cycles, as evidenced by the sustained 1.0 V plateau.

To further investigate the contribution of $Ca[B(hfip)_4]_2$ to the SKB cathode, three-electrode cell tests were conducted using Mg metal as a reference electrode. Figure 3c presents the CV profiles of the Mg–S cell with pure Mg electrolyte. During the first cathodic sweep, the primary reduction peak of sulfur appeared at 1.15 V, while the anodic peak was observed at 1.85 V in the reverse anodic sweep, a consistent behavior with the previous study.[24] In subsequent CV cycles, both the cathodic and anodic peaks shifted slightly to higher potentials, aligning with the galvanostatic discharge/charge profiles, which exhibited a slight voltage increase after the first cycle. Additionally, small shoulder signals in the CVs around 0.5 V suggest the presence of the latter-stage sulfur redox reactions. With the 0.3 M $Mg[B(hfip)_4]_2 + 0.15$ M $Ca[B(hfip)_4]_2$/DME electrolyte (Figure 3d), which exhibited unfavorable charge behavior in two-electrode cells (Figure S9c, Supporting Information), additional cathodic and anodic peaks were observed compared to the pure Mg electrolyte (Figure 3c). During the first cathodic scan, two reduction peaks appeared at 1.30 and 0.96 V, corresponding to the discharge profile (Figure S9c, Supporting Information). Note that the first reduction peak position was higher than that of the pure Mg electrolyte, suggesting that the first-stage sulfur-to-polysulfide redox reaction was also facilitated by $Ca[B(hfip)_4]_2$. During the first anodic reaction, two oxidation peaks, not present in the two-electrode cell, were observed, indicating the reversible two-step sulfur redox reaction accelerated by Ca^{2+} addition. In subsequent CV cycles, the cathodic peaks shifted slightly to higher potentials, aligning with the galvanostatic discharge profiles, while the two anodic peaks gradually merged within the 1.6–2.0 V range.

Overall, $Ca[B(hfip)_4]_2$ additives significantly improved sulfur redox reaction kinetics, particularly in the latter stages of sulfur redox reactions. Even though cathodic performance improved with increasing Ca^{2+} concentrations, the practical two-electrode cells did not achieve full-cell performance at higher Ca^{2+} concentrations due to excessive anode overvoltage in the first cycle. This was shown in Figure 3a and higher charge voltage was observed with higher Ca^{2+} concentrations. In two-electrode full-cell tests, an appropriate $Ca[B(hfip)_4]_2$ concentration is 0.05 M. Further investigations hereafter were conducted using the 0.3 M $Mg[B(hfip)_4]_2 + 0.05$ M $Ca[B(hfip)_4]_2$/DME electrolyte.

A mechanistic investigation of sulfur redox in the presence of $Ca[B(hfip)_4]_2$ in the electrolyte was further conducted using SEM-EDX and X-ray photoelectron spectroscopy (XPS). Firstly, the Ca^{2+} contribution to the sulfur redox was quantified through SEM-EDX at different discharge/charge plateaus (**Figure 4**a). After

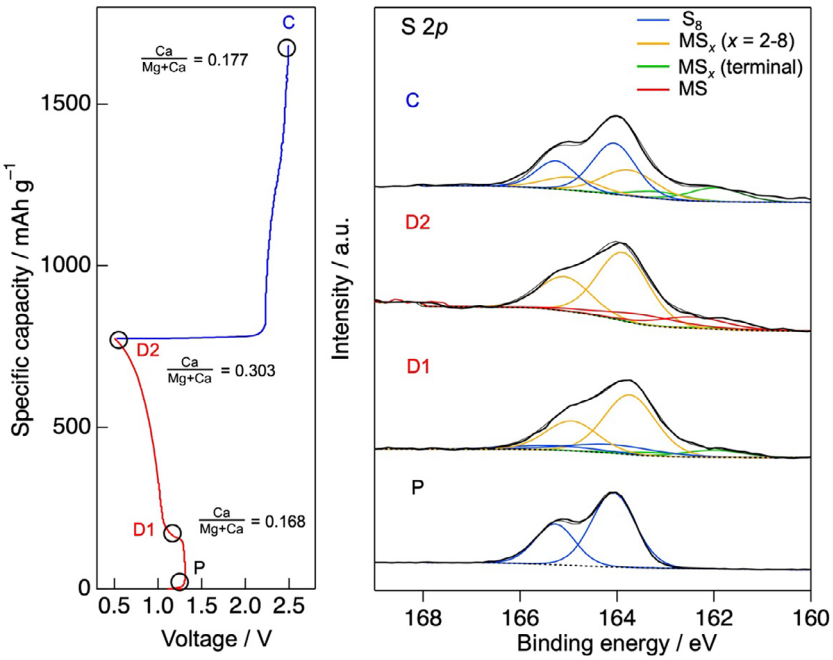

Figure 4. a) Charge–discharge profile of Mg–S cells 0.3 M $Mg[B(hfip)_4]_2 + 0.05$ M $Ca[B(hfip)_4]_2$/DME and SEM-EDX analysis. b) S 2*p* XPS spectra of SKB cathode at different states of discharge and charge.

the first discharge plateau (D1, 160 mAh g^{-1}), the molar ratio of Ca/(Mg + Ca) in (poly)sulfides was calculated to be 0.168, indicating that the majority of the discharged capacity originated from Mg. This ratio is nearly identical to the electrolyte composition (Ca/(Mg + Ca) = 0.143), suggesting that Mg^{2+} and Ca^{2+} participated in sulfur redox reactions in accordance with their respective activities during the D1 stage.

However, from D1 to D2 (latter discharge state, 615 mAh g^{-1}), the Ca^{2+} contribution increased compared to D1, suggesting that Ca^{2+} likely participated in the latter stages of the sulfur redox reaction.

Figure 4b presents the S 2*p* XPS spectra during discharge and charge. A doublet peak (S $2p_{3/2}$: 164 eV) corresponding to elemental sulfur (S_8) is observed in the pristine state (P). During discharge, the peaks almost disappeared, while doublet peaks were observed; they are attributed to polysulfides (MS_x, $x = 2–8$, S $2p_{3/2} = 163.5$ eV), monosulfide (MS, S $2p_{3/2} = 162.5$ eV), and terminal sulfur atoms in polysulfides (S $2p_{3/2} = 161.8$ eV), based on the previous study.[23] At the D1 state, the sulfur species were predominantly in the polysulfide state, as indicated by the MS_x peaks and the corresponding terminal sulfur peaks of MS_x, with a slight amount of pristine S_8. At the fully discharged (D2) state, the remaining elemental sulfur peaks disappeared, instead, the monosulfide MS, the fully reduced form, was detected. Even though the peak separation between MgS and CaS is challenging and cannot be quantitatively analyzed, the contribution of Ca^{2+} was found to be substantial (30.3%), as discussed earlier. Interestingly, not only Ca^{2+}, but also a significant proportion of Mg^{2+} participated in the latter stage of the sulfur redox reaction, leading to the formation of MS. This suggests that the presence of Ca polysulfides facilitated the subsequent redox reaction of polysulfides with Mg^{2+}, a phenomenon that was not observed when using a pure Mg electrolyte, possibly indicating that the presence of Ca^{2+} enhances the reaction kinetics between Mg^{2+} and disulfide species, as also evidenced by the rise in the second plateau potential (Figure S9b, Supporting Information).

In the charged state (C), the MS peak disappeared, while the elemental sulfur peak became predominant, indicating that sulfur underwent semi-reversible redox reactions with the Mg–Ca hybrid electrolyte. The amounts of Mg and Ca during the redox process were semi-quantitatively estimated from Mg 2*p* and Ca 2*p* XPS spectra (Figure S11, Supporting Information). Considering the remaining Mg and Ca after charging, the Ca^{2+} contribution decreased from D2 to the charged (C) state (0.303–0.177), suggesting that the reversible sulfur conversion is more favorable with Ca^{2+}.This reversibility could be attributed to thermodynamical favorability of Ca^{2+} in Mg–Ca hybrid systems as mentioned in introduction section.

2.3. Improved Capacity Retention with Single-Nanosized α-MnO_2 Modified Separator

Despite the enhanced anodic and cathodic performance facilitated by Ca^{2+}, significant capacity decay and early short-circuiting occurred, primarily due to polysulfide migration to the anode and the subsequent formation of a polysulfide-based passivation layer. This layer leads to inhomogeneous Mg deposition, ultimately resulting in an early short circuit as shown in Figure S12, Supporting Information. Since the formation of the passivation layer on anode could be linearly proportional to the polysulfide species, Mg–Ca hybrid electrolyte causes early short-circuit despite of high discharge capacity.

To improve cycling stability, we modified the GF/C separator with ultrasmall α-MnO_2 nanoparticles. Using an in situ modification process with an alcohol solution, the nanoparticles could be directly incorporated without any binders. As shown in Figure S13a–c, Supporting Information, the in situ modification process resulted in a homogeneously dispersed ultrasmall α-MnO_2 layer, as confirmed by the broad XRD patterns of α-MnO_2. The modified ultrasmall α-MnO_2 formed a network of ≈2 μm-sized particles, which effectively tangled with the glass fiber separator. Additionally, the weight of the modified separator averaged 9.8 mg, compared to 10.8 mg for the pure GF/C separator, indicating that the liquid-phase modification process led to a slight loss of GF/C material, while incorporating only a small amount of ultrasmall α-MnO_2.

As shown in Figure S14a, Supporting Information, the ultrasmall α-MnO_2-modified GF/C enabled a longer first discharge plateau compared to the bare GF/C, which may be attributed to suppressing sulfur self-discharge, as previously reported.[40] In the second and third cycles, the capacity decreased significantly; however, in the subsequent cycles, the capacity remained stable (Figure S14b, Supporting Information). This suggests that while α-MnO_2-modified GF/C effectively prevents polysulfide migration, it is less effective in suppressing polysulfide dissolution.

To understand the mechanism for suppressing polysulfide migration, MgS_x/DME solution was chemically synthesized based on a previous study,[23] and its adsorption activity with ultrasmall α-MnO_2 was investigated. One hour after immersing 10 mg of ultrasmall α-MnO_2 into 2 mL of MgS_x/DME solution, the yellowish color disappeared, suggesting that polysulfides were absorbed onto the ultrasmall α-MnO_2, as shown in Figure S15a, Supporting Information. XPS analysis (Figure S15b–d, Supporting Information) revealed that sulfur species were adsorbed on the surface of α-MnO_2, with a portion of sulfur being oxidized, as indicated by the appearance of SO_x peaks in the S 2*p* spectrum. Furthermore, in the O 1*s* spectrum, the abundance of oxygen defects on the α-MnO_2 surface decreased, and the Mn 2*p* spectrum shifted to a higher binding energy. These observations indicate that polysulfides were adsorbed primarily onto oxygen defect sites at the α-MnO_2 surface, leading to Mn oxidation.

This polysulfide adsorption mechanism, which utilizes surface oxygen defects, is similar to the role of α-MnO_2 previously reported in Li–S battery systems.[41]

Finally, we combined our developed technique to extend the cycle life of Mg–S cells, i.e., the Mg–Ca hybrid electrolyte and the α-MnO_2-modified GF/C. As shown in **Figure 5**a, the first discharge capacity exceeded 1000 mAh g^{-1}, with an extended first voltage plateau at 1.15 V. However, complete charging was not achieved, leading to a capacity fade in subsequent cycles. Despite this, the modified separator significantly improved cycling stability with Mg–Ca hybrid electrolyte, extending

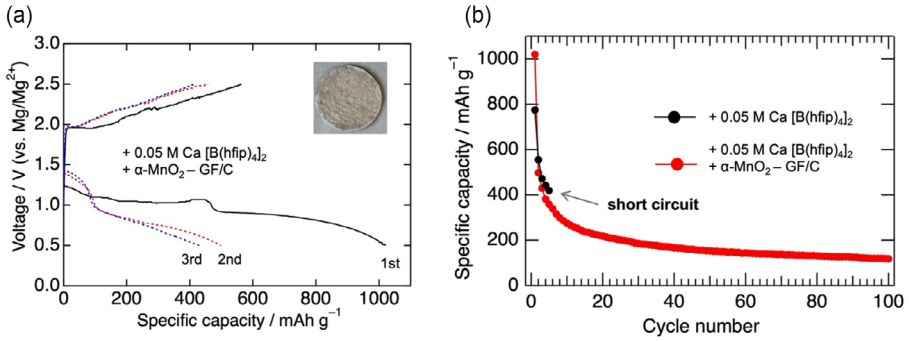

Figure 5. a) Charge–discharge profile and b) cycle performance of Mg–S cells with 0.3 M $Mg[B(hfip)_4]_2$ + 0.05 M $Ca[B(hfip)_4]_2$/DME electrolyte and α-MnO_2-modified GF/C separator.

the cycle life from 5 cycles to over 100 cycles, maintaining the higher capacity as shown Figure 5b. This indicated that ultrasmall α-MnO_2-modified separator outperforms carbon-coated separators without increasing the separator's weight, while achieving performance comparable to Mo_6S_8-modified separators.[23]

3. Conclusion

Incorporating $Ca[B(hfip)_4]_2$ into an $Mg[B(hfip)_4]_2$-based electrolyte significantly enhances Mg–S battery performance. On the Mg anode side, the presence of Ca^{2+} alters Mg re-plating behavior on the anode, promoting the formation of thicker, plate-like Mg deposits that remain smooth and well-adhered to the stripped sites. This shift in Mg deposition kinetics helps stabilize the anode interface and reduce overall cell polarization, contributing to long-term cycling stability. On the sulfur cathode side, the Mg–Ca hybrid electrolyte increases the second discharge plateau potential and significantly improves discharge capacity, indicating an accelerated solid-to-solid conversion of disulfide to sulfide. In addition to the electrolyte, the separator modification also improves the high capacity and the long cycle life. An in situ modified GF/C separator with ultrasmall α-MnO_2 exhibits strong polysulfide adsorption, effectively suppressing polysulfide migration. As a result, the Mg–S cells achieved capacities exceeding 1000 mAh g^{-1} and remained stable for over 100 cycles. This synergistic strategy of combining a Mg–Ca hybrid electrolyte with an α-MnO_2-modified separator can be easily incorporated with advanced sulfur cathode design, offering a practical route to further enhance Mg–S battery performance. Moreover, this strategy is broadly applicable and can be extended to other Mg-based battery systems, including Mg–oxide and Mg–sulfide batteries. From the viewpoint of sustainability, incorporating abundant Ca resources into Mg electrolytes represents an outstanding approach, offering not only superior battery performance but significant ripple effects toward developing rare metal-free storage batteries that avoid reliance on Li. We believe our findings provide a promising pathway for the design of high-energy-density, sustainable magnesium-based energy storage systems.

4. Experimental Section

Preparation of S/KB/C (50 wt%: 30 wt%: 10 wt%) Cathode Electrodes

1.3 g of sulfur and 0.78 g of Ketjenblack (KB) were firstly mixed using a mortar for 15 min and then ball-milled at 500 rpm for 15 min using SiN balls. Afterward, 0.208 g of Super P was added to the milling pot and further ball-milled at 250 rpm for 15 min. Note that the ratio of the composite to SiN ball is 1 wt%: 25 wt%. The cathode electrode was prepared by adding 90 mg of S/KB/C composite to the mixture of 0.8 mL of cyrene (dihydrolevoglucosenone) solution containing 10 mg of PVDF-HFP (poly(vinylidene + fluoride-hexafluoropropylene)) and 0.8 mL pure cyrene solution and blended for 20 min. The resulting slurry, composed of 50 wt% sulfur, was then casted onto carbon coated Al foil. The dried electrode was cut into a 12 mm-diameter disk with a sulfur mass loading of ≈1.0 mg cm^{-2}. This prepared electrode was further dried at 313 K under vacuum for 12 h and transferred to an argon-filled glove box.

Fabrication of Glass Fiber Separators with Incorporated Ultrasmall α-MnO_2

Ultrasmall α-MnO_2-modified separators were fabricated using a modified alcohol solution process and an alcohol reduction process, as previously reported.[29] For the preparation of nano α-MnO_2-modified separators, denoted as α-MnO_2@GF/C, manganese chloride tetrahydrate (4.550 mmol) was first dissolved in 125 mL of isopropanol to form solution A. Subsequently, 30 pieces of 16 mm ø disk-shaped GF/C were immersed in solution A and stirred for 30 min.

Sodium permanganate monohydrate (3.175 mmol) and ammonium chloride (6.350 mmol) were then dissolved in 16.5 mL of acetonitrile containing 1.5 mL of deionized water to prepare solution B. Solution B was gradually added dropwise to solution A under gentle stirring, leading to the formation of a brown colloidal precipitate. The mixture was then refluxed for 1 h. The modified GF/C separators were collected, thoroughly washed with ethanol, and dried overnight at 70 °C under vacuum.

Synthesis of MgS_x/Dimethoxyethane(DME) Solution

The MgS_x/DME solution was prepared with minor modifications based on a previously reported method.[23] Sulfur and magnesium metal powder (in an 8:1 molar ratio) were first ball-milled under an Ar atmosphere at 200 rpm for 10 h. The resulting mixture was then added to 40 mL of DME and refluxed for 12 h under Ar atmosphere, yielding a transparent yellowish solution.

Cell Assembly

For preparation of anodes, a 14 mm-diameter disk of Mg foil (thickness: 0.1 mm) was carefully polished to eliminate any Mg oxides films in an argon-filled glove box. Regarding the electrolyte, $Mg[B(hfip)_4]_2$ and $Ca[B(hfip)_4]_2$ (hfip: hexafluoroisopropyl) were synthesized following the procedure described in the prior publication.[26,33] The cathode, anode, and DME-electrolyte solution (80 μL) were assembled in a 2032-type coin cell using two glass-fiber separators (16 mm diameter, GF/C).

Characterizations

XRD analysis was conducted with a Bruker D2 PHASER XE-T Edition with a Cu Kα source. SEM and energy-dispersive X-ray spectroscopy (EDX) were performed using a (JSM-IT510) with EDX detector (JED-2300 Analysis Station Plus) from JEOL. X-ray photoelectron spectroscopy (XPS) measurements were carried out on a Specs XPS system with a Phoibos 150 energy analyzer using monochromatic Al Kα radiation (1486.6 eV). CasaXPS was used for data analysis. The samples were transferred under Ar from the glovebox to the XPS system to avoid air contamination.

Electrochemical Tests

Symmetric (Mg||Mg), asymmetric (Mg||Cu, Mg||SS), and Mg-S battery cells were conducted in a 2032-type coin cells with 14 mm diameter Mg foil, 14 mm diameter Cu foil, and 14 mm diameter SUS316L foil using a Bio-Logic VMP3 potentiostat and a TOSCAT system (TOYO SYSTEM CO., LTD.). For the three-electrode Mg–S battery tests, SB7 cell (EC FRONTIER) was used, consisting of a 16 mm diameter Mg foil as the counter electrode, an 18 mm-diameter Mg ring as the reference electrode, and a 12 mm-diameter SKB cathode as a working electrode. The electrolyte volume was fixed at 200 μL. The three-electrode tests were performed using a Bio-Logic VMP3 potentiostat.

Acknowledgements

Parts of this work were supported by CELEST (Center for Electrochemical Energy Storage Ulm-Karlsruhe), German Research Foundation (DFG) under Project ID 390874152 (POLiS Cluster of Excellence), the Federal Ministry of Education and Research (Bundesministerium für Bildung und Forschung, BMBF) of Germany within the project "CaSino" (03XP0487F), JSPS KAKENHI (23KJ0214), the Light Metal Educational Foundation, International Joint Graduate Program in Materials Science: GP-MS at Tohoku University, and Cooperative Research Program of NJRC Mater. & Dev. (MEXT), Japan.

Conflict of Interest

The authors declare no conflict of interest.

Data Availability Statement

The data that support the findings of this study are available from the corresponding author upon reasonable request.

Keywords: hybrid electrolytes · magnesium batteries · magnesium sulfur batteries · manganese oxides

[1] J. M. Tarascon, M. Armand, *Nature* **2001**, *414*, 359.
[2] J. Muldoon, C. B. Bucur, T. Gregory, *Angew. Chem., Int. Ed.* **2017**, *56*, 12064.
[3] C. B. Bucur, T. Gregory, A. G. Oliver, J. Muldoon, *J. Phys. Chem. Lett.* **2015**, *6*, 3578.
[4] H. D. Yoo, I. Shterenberg, Y. Gofer, G. Gershinsky, N. Pour, D. Aurbach, *Energy Environ. Sci.* **2013**, *6*, 2265.
[5] C.-X. Zu, H. Li, *Energy Environ. Sci.* **2011**, *4*, 2614.
[6] W. Yao, K. Liao, T. Lai, H. Sul, A. Manthiram, *Chem. Rev.* **2024**, *124*, 4935.
[7] G. Bieker, V. Küpers, M. Kolek, M. Winter, *Commun. Mater.* **2021**, *2*, 37.
[8] Y. Son, J.-S. Lee, Y. Son, J.-H. Jang, J. Cho, *Adv. Energy Mater.* **2015**, *5*, 1500110.
[9] K. D. Collins, *Biophys. J.* **1997**, *72*, 65.
[10] Z. Zhao-Karger, X. Zhao, D. Wang, T. Diemant, R. J. Behm, M. Fichtner, *Adv. Energy Mater.* **2015**, *5*, 1401155.
[11] Y. Yang, W. Wang, Y. Nuli, J. Yang, J. Wang, *ACS Appl. Mater. Interfaces* **2019**, *11*, 9062.
[12] J. Häcker, D. H. Nguyen, T. Rommel, Z. Zhao-Karger, N. Wagner, K. A. Friedrich, *ACS Energy Lett.* **2022**, *7*, 1.
[13] Y. Yang, W. Fu, D. Zhang, W. Ren, S. Zhang, Y. Yan, Y. Zhang, S.-J. Lee, J.-S. Lee, Z.-F. Ma, J. Yang, J. Wang, *ACS Nano* **2023**, *17*, 1255.
[14] A. Du, Z. Zhang, H. Qu, Z. Cui, L. Qiao, L. Wang, J. Chai, T. Lu, S. Dong, T. Dong, H. Xu, X. Zhou, G. Cui, *Energy Environ. Sci.* **2017**, *10*, 2616.
[15] P. Li, R. Razaq, S.-H. Bo, *ACS Appl. Energy Mater.* **2024**, *7*, 11343.
[16] Z. Zhao-Karger, R. Liu, W. Dai, Z. Li, T. Diemant, B. P. Vinayan, C. Bonatto Minella, X. Yu, A. Manthiram, R. J. Behm, M. Ruben, M. Fichtner, *ACS Energy Lett.* **2018**, *3*, 2005.
[17] L. Wang, T. Diemant, Z. Li, B. Dasari, Z. Zhao-Karger, *ACS Appl. Energy Mater.* **2023**, *6*, 1008.
[18] R. Razaq, P. Li, Y. Dong, Y. Li, Y. Mao, S.-H. Bo, *EcoMat* **2020**, *2*, e12056.
[19] Z. Li, A. Welle, S. Vincent, L. Wang, S. Fuchs, S. Riedel, A. Roy, D. Bosubabu, J. M. García-Lastra, M. Fichtner, Z. Zhao-Karger, *Adv. Energy Mater.* **2023**, *13*, 2302905.
[20] X. Zhao, Y. Yang, Y. NuLi, D. Li, Y. Wang, X. Xiang, *Chem. Commun.* **2019**, *55*, 6086.
[21] X. Zhou, J. Tian, J. Hu, C. Li, *Adv. Mater* **2018**, *30*, 1704166.
[22] T. Gao, M. Noked, A. J. Pearse, E. Gillette, X. Fan, Y. Zhu, C. Luo, L. Suo, M. A. Schroeder, K. Xu, S. B. Lee, G. W. Rubloff, C. Wang, *J. Am. Chem. Soc.* **2015**, *137*, 12388.
[23] L. Wang, P. Jankowski, C. Njel, W. Bauer, Z. Li, Z. Meng, B. Dasari, T. Vegge, J. M. G. Lastra, Z. Zhao-Karger, M. Fichtner, *Adv. Sci.* **2022**, *9*, 2104605.
[24] Y. Ji, X. Liu-Théato, Y. Xiu, S. Indris, C. Njel, J. Maibach, H. Ehrenberg, M. Fichtner, Z. Zhao-Karger, *Adv. Funct. Mater.* **2021**, *31*, 2100868.
[25] X. Yu, A. Manthiram, *ACS Energy Lett.* **2016**, *1*, 431.
[26] Z. Li, O. Fuhr, M. Fichtner, Z. Zhao-Karger, *Energy Environ. Sci.* **2019**, *12*, 3496.
[27] Y. Li, D. Ye, W. Liu, B. Shi, R. Guo, H. Zhao, H. Pei, J. Xu, J. Xie, *ACS Appl. Mater. Interfaces* **2016**, *8*, 28566.
[28] J. Zu, W. Jing, X. Dai, Z. Feng, J. Sun, Q. Tan, Y. Chen, Y. Liu, *J. Alloys Compd.* **2023**, *933*, 167767.
[29] R. Iimura, S. Kawasaki, T. Yabu, S. Tachibana, K. Yamaguchi, T. Mandai, K. Kisu, N. Kitamura, Z. Zhao-Karger, S. Orimo, Y. Idemoto, M. Matsui, M. Fichtner, I. Honma, T. Ichitsubo, H. Kobayashi, *Small* **2025**, *21*, 2411493.
[30] Z. Zhao-Karger, M. E. Gil Bardaji, O. Fuhr, M. Fichtner, *J. Mater. Chem. A* **2017**, *5*, 10815.
[31] O. Tutusaus, R. Mohtadi, N. Singh, T. S. Arthur, F. Mizuno, *ACS Energy Lett.* **2017**, *2*, 224.
[32] T. Mandai, U. Tanaka, M. Watanabe, *Energy Storage Mater.* **2024**, *67*, 103302.
[33] T. Mandai, *ACS Appl. Mater. Interfaces* **2020**, *12*, 39135.
[34] G. Wang, X. Liu, H. Shi, Y. Ma, Z. Wang, C. Sun, F. Song, Z. Zhang, S. Dong, M. Sun, A. Du, G. Cui, *ACS Energy Lett.* **2024**, *9*, 48.
[35] M. Matsui, *J. Power Sources* **2011**, *196*, 7048.
[36] J. Bi, Z. Zhou, J. Li, B. Li, X. Sun, Y. Liu, K. Wang, G. Gao, Z. Du, W. Ai, W. Huang, *Angew. Chem., Int. Ed.* **2024**, *63*, e202407770.

[37] F. Hao, A. Verma, P. P. Mukherjee, *J. Mater. Chem. A* **2019**, *7*, 18442.
[38] Y. Ji, H. Sun, Z. Li, L. Ma, W. Zhang, Y. Liu, L. Pan, W. Mai, J. Li, *J. Mater. Chem. A* **2022**, *10*, 25539.
[39] T. Luo, Y. Wang, B. Elander, M. Goldstein, Y. Mu, J. Wilkes, M. Fahrenbruch, J. Lee, T. Li, J. L. Bao, U. Mohanty, D. Wang, *Adv. Mater* **2024**, *36*, 2306239.
[40] D. Bosubabu, Z. Li, Z. Meng, L.-P. Wang, M. Fichtner, Z. Zhao-Karger, *J. Mater. Chem. A* **2021**, *9*, 25150.
[41] Y.-T. Gao, X.-Y. Wang, D.-Q. Cai, S.-Y. Zhou, S.-X. Zhao, *ACS Appl. Mater. Interfaces* **2023**, *15*, 30152.

Manuscript received: May 14, 2025
Revised manuscript received: June 5, 2025
Version of record online: